Direct Exfoliation of Nanoribbons from Bulk van der Waals Crystals

Ashley P. Saunders, Victoria Chen, Jierong Wang, Qitong Li, Amalya C. Johnson, Amy S. McKeown-Green, Helen J. Zeng, T. Kien Mac, M. Tuan Trinh, Tony F. Heinz, Eric Pop, and Fang Liu*

Confinement of monolayers into quasi-1D atomically thin nanoribbons could lead to novel quantum phenomena beyond those achieved in their bulk and monolayer counterparts. However, current experimental availability of nanoribbon species beyond graphene is limited to bottom-up synthesis or lithographic patterning. In this study, a versatile and direct approach is introduced to exfoliate bulk van der Waals crystals as nanoribbons. Akin to the Scotch tape exfoliation method for producing monolayers, this technique provides convenient access to a wide range of nanoribbons derived from their corresponding bulk crystals, including MoS_2, WS_2, $MoSe_2$, WSe_2, $MoTe_2$, WTe_2, ReS_2, and hBN. The nanoribbons are predominantly monolayer, single-crystalline, parallel-aligned, flat, and exhibit high aspect ratios. The role of confinement, strain, and edge configuration of these nanoribbons is observed in their electrical, magnetic, and optical properties. This versatile exfoliation technique provides a universal route for producing a variety of nanoribbon materials and supports the study of their fundamental properties and potential applications.

1. Introduction

Facile and versatile preparation methods are paramount in the development of any emerging class of quantum materials. A prime example is the Scotch tape exfoliation technique, which launched the field of two-dimensional (2D) materials.[1] This tape exfoliation acts as a universal top-down strategy that separates nearly any bulk van der Waals (vdW) crystal into its monolayer counterparts. It grants access to a diverse spectrum of atomically thin materials, whose experimental availabilities led to numerous breakthroughs in the fundamental research of 2D physics. When 2D materials are further engineered as one-dimensional (1D) nanoribbons, the 1D lateral confinement and edge states strongly influence the band structure, transport, and electronic transitions.[2] As a result, nanoribbons are predicted to manifest a spectrum of different properties including emergent magnetism, topological phase transitions, spin density waves, and catalytic activity.[3–5]

Nanoribbon materials also enable the study of electronic, optoelectronic, magnetic, and thermoelectric properties of confined materials depending on their width, edge structures, and strain. For instance, hexagonal boron nitride (hBN) is an insulator with a wide band gap ($\approx$6 eV), while edge states can yield hBN nanoribbons with semiconducting or metallic character.[6,7] Transition metal dichalcogenides (TMDCs), such as MoS_2, are semiconductors and nonmagnetic in both bulk and monolayer form. In contrast, first-principles calculations have predicted that TMDC nanoribbons with zigzag edges should be metallic and ferromagnetic,[3,8,9] while nanoribbons with armchair edges are nonmagnetic and semiconducting.[3,9]

Despite numerous theoretical studies on the properties of various quasi-1D structures, existing experimental demonstrations have primarily focused on graphene nanoribbons. A broad variety of nanoribbons, especially those beyond graphene, remain relatively underexplored. Current techniques for nanoribbon production can be categorized into top-down or bottom-up approaches.

Top-down methods primarily use the unzipping of nanotubes, or they use lithography and etching techniques to produce striped patterns out of monolayers. Examples include

A. P. Saunders, A. S. McKeown-Green, H. J. Zeng, F. Liu
Department of Chemistry
337 Campus Drive, Stanford, CA 94305, USA
E-mail: fliu10@stanford.edu

V. Chen, E. Pop
Department of Electrical Engineering
476 Lomita Mall, Suite 102, Stanford, CA 94305, USA

J. Wang, Q. Li, T. F. Heinz, E. Pop
Department of Applied Physics
348 Via Pueblo Mall, Stanford, CA 94305, USA

J. Wang, Q. Li, T. F. Heinz, E. Pop
SLAC National Accelerator Laboratory
2575 Sand Hill Road, Menlo Park, CA 94025, USA

A. C. Johnson, E. Pop
Department of Materials Science and Engineering
Stanford, CA 94305, USA

T. K. Mac, M. T. Trinh
Department of Chemistry and Biochemistry
Utah State University, Logan, UT 84322, USA

E. Pop
Precourt Institute for Energy
Stanford University, Stanford, CA 94305, United States

**ADVANCED
SCIENCE NEWS**

www.advancedsciencenews.com

**NANO · MICRO
small**

www.small-journal.com

electron-beam lithography,[10] dry/wet etching,[11,12] scanning probe lithography,[13,14] direct helium ion-beam milling,[15] ionic scissoring of macroscopic crystals,[16] and liquid phase etching with a reducing agent through a mechano-chemical process.[17] However, the substantial costs associated with purchasing, installing, maintaining, and optimizing the operating conditions of such equipment restrict widespread use throughout research institutions. Additionally, the processes of writing, resist patterning, and lift-off stages can compromise the structural and chemical integrity of delicate 2D crystalline materials, which may result in nanoribbons with rough edges and low crystal quality.

On the other hand, bottom-up techniques emphasize directed growth or chemical reactions to synthesize nanoribbons. Strategies include molecular beam epitaxy,[18,19] guided growth within carbon nanotubes,[20] growth along substrate crystal atomic alignments/steps/edges,[21–25] and growth with moving catalyst droplets.[26] To date, only a limited selection of monolayer nanoribbons from the diverse 2D library has been successfully synthesized, and these techniques lack control over size, shape, and adaptability to a broad material selection. The development of a *universal*, scalable, and non-destructive production technique for a broad variety of nanoribbons is highly desired.

Here, we introduce a universal, reproducible, and large-scale top-down exfoliation technique to achieve parallel-aligned and single-crystalline 2D nanoribbons directly from bulk crystals. The exfoliation approach is built upon the strong adhesion of metals on monolayers,[27,28] and vicinal surfaces that are a common configuration on vdW bulk crystals. The ability to obtain nanoribbons directly from an extensive range of vdW bulk materials will facilitate the exploration and manipulation of the distinct electrical, magnetic, or optical properties in 1D or quasi-1D geometry. The results could be instrumental for further breakthroughs that encompass characteristics beyond those currently explored in monolayer materials.

2. Exfoliation of Nanoribbons from Bulk Crystals

2.1. Modified Tape Exfoliation

A schematic of our exfoliation technique is illustrated in **Figure 1**. The slanted surfaces of bulk vdW crystals usually exhibit a step-wise pattern with a non-zero polar cut angle, θ, termed the vicinal surface (as depicted in Figure 1a,b, and S2). To initiate the exfoliation of monolayer nanoribbons, a 100-nm layer of gold (Au) is evaporated onto the vicinal surfaces, followed by a spin-coated polyvinylpyrrolidone (PVP) layer to prevent contamination. The deposition rate was tuned to be low enough to maintain a relatively high-quality TMDC monolayer.[29] When the gold layer is lifted with a rigid and flat thermal release tape (TRT), it effectively exfoliates monolayer steps from the bulk crystal surface in the form of aligned nanoribbons. The TRT/PVP/Au/nanoribbon assembly is subsequently transferred onto a destination substrate, such as SiO$_2$/Si, sapphire, or fused silica. Removal of TRT with heating and dissolving the PVP in water leaves a clean Au layer, which is then etched using KI/I$^-$ solution. This etching process is mild and preserves the integrity of many 2D materials.[27,28] After a secondary cleaning with water, flat and parallel aligned nanoribbons are obtained on the chosen substrate (Figure 1c).

Our method allows for repeated metal deposition and exfoliation on the same vicinal surface multiple times, and benefits from high exfoliation yield. The enhanced yield and high-throughput originate from the substantial binding and adsorption energies of Au on 2D monolayers, which can effectively counteract the interlayer vdW force of a variety of bulk crystals.[28,30,31] As a result, Au can be employed as a universal exfoliation scaffold for both large-area monolayers and striped nanoribbons. Despite the use of Au as an exfoliation medium, X-ray Photoelectron Spectroscopy (XPS) analysis confirms that Au is removed to an undetectable level after etching (Figure S2, Supporting Information), validating cleanliness of the nanoribbon crystal surface.

This technique allows us to exfoliate a diverse array of nanoribbons directly from their corresponding vdW bulk crystals (**Figure 2**), ranging from semiconducting TMDCs to insulating hBN. Notably, these monolayer nanoribbons preserve the flatness, parallel alignment, straight edges, and single-crystalline nature of their initial bulk crystal surfaces. They feature very high aspect ratios, including widths varying from 20 nm to several hundreds of nanometers and lengths extending up to the millimeter scale. The dimensions of these ribbons, incorporating their length, width, and spacing, directly correlate with the length, width, and height of the original crystal steps present on the vicinal surface (Figure 1b). The quality, transferability, and efficiency of this technique stand in contrast to existing fabrication and synthesis techniques which often face challenges in large-scale nanoribbon production, transferring ribbons from their growth substrates for device integration, and/or compatibility with a diverse range of 2D materials.

3. Survey of Emergent Nanoribbon Properties

3.1. Width- and Strain-Dependent Optical Properties in Exfoliated WSe$_2$ Nanoribbons

Our TMDC nanoribbons exhibit photoluminescence (PL) that covers a spectrum from the visible to the near-infrared range, comparable to their monolayer counterparts (**Figure 3**). Figure 3a and Figure 3b compare the PL from exfoliated WSe$_2$ nanoribbons of widths varying from hundreds of nanometers down to tens of nanometers. To establish a more direct comparison with TMDC monolayers, we employed the top-down exfoliation technique to obtain monolayers and nanoribbons from the same vdW bulk crystal. As shown in Figure 3b, despite the distribution of PL peak positions over different ribbon widths, PL peak positions of the nanoribbons are still located within the wide distribution of emissions in their monolayer equivalents, albeit shifted slightly toward the higher energy end. Previous studies on MoS$_2$ nanoribbons synthesized on Si(001) surfaces pre-treated with phosphine and through controlled O$_2$ etching of monolayers observe similar PL blueshifts up to 70 meV when the nanoribbon width was reduced below 50 nm.[21,32] Our observed trend of a PL blueshift in narrower nanoribbon widths is consistent amongst differing production methods. However, the trend opposes the anticipated redshift that is often induced by defects, while the width of ribbons (at tens of nanometers) is greater than the exciton Bohr radius in the quantum confinement regime.
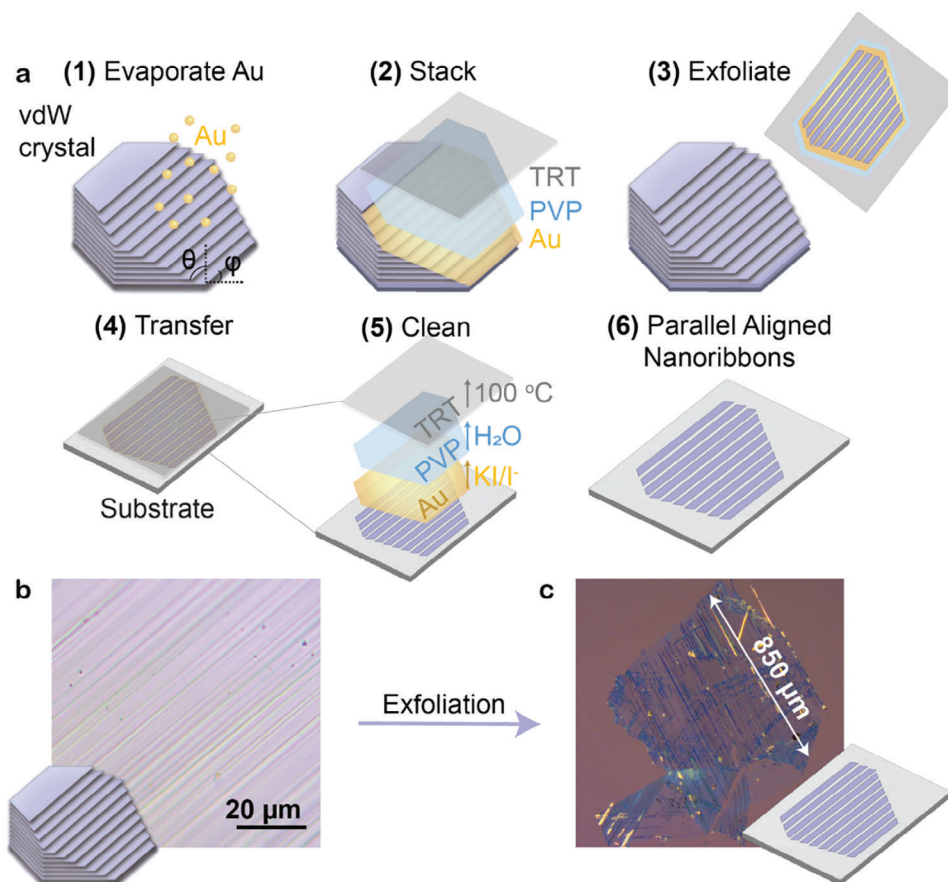
Figure 1. Nanoribbon exfoliation from the vicinal surface of bulk vdW crystals. a) Schematic illustration of the top-down exfoliation technique to obtain single crystalline nanoribbons: 1) deposit gold onto a bulk vdW crystal with exposed vicinal regions; 2) spin-coat with a layer of polyvinyl pyrrolidone (PVP) and apply thermal release tape (TRT); 3) pick up the TRT/PVP/Au/nanoribbon stack from the crystal and 4) place the stack onto the destination substrate; 5) remove the TRT by heating at 100 °C, rinse with water to dissolve the sacrificial PVP layer, and etch gold away in KI/I⁻ etchant solution; 6) obtain parallel aligned single crystalline nanoribbons. b) Optical image of an exemplary vicinal surface on a bulk WSe_2 crystal. c), Optical image of a large area of continuous $MoSe_2$ nanoribbons on a 90 nm SiO_2/Si substrate.

A possible mechanism for the observed blueshift is compressive strain.[33] As shown in Figure 3c, the E′ Raman mode for WSe_2 nanoribbons (253.1 cm⁻¹) resides at a slightly higher frequency than the same mode in monolayer flakes (252.7 cm⁻¹) exfoliated from the same crystal. This shift is consistent among multiple locations of WSe_2 monolayer and nanoribbons (Figure S3, Supporting Information). In WSe_2 monolayers, a shift of the E′ Raman peak by 0.46 cm⁻¹ to higher frequency correlates to a compressive strain of 1.62% on average, as estimated in strained WSe_2 monolayers.[34] The strain appears to be particularly pronounced as a 2D lattice is reduced into 1D structures, indicating that narrow ribbons can be more susceptible to mechanical deformation.

Lastly, exfoliated nanoribbons exhibit an anisotropic second harmonic generation (SHG) polarization response (purple curve in Figure 3d) that is distinct from their monolayer counterparts. TMDC monolayers have significant second-order nonlinear optical susceptibility and can be used for effective nonlinear light processing such as frequency up/down conversion. Typical TMDC monolayers exhibit a symmetrical second harmonic generation (SHG) response as a function of the polarization of the pump

beam, reflecting the symmetry of the hexagonal crystal lattices (see yellow curve in Figure). In comparison, 1D nanoribbon structures made from TMDC materials create a more strongly anisotropic optical excitation, as a consequence of screening of the electric field perpendicular to the edges of the nanoribbons Therefore, an extrinsic anisotropy is induced in the created nonlinear source polarization. Radiation from the nonlinear source polarization at the second harmonic frequency is also influenced by the same dielectric screening effect, further enhancing the anisotropy of the SHG signal). We note that such effects afford configurable and versatile control of the far-field amplitude and polarization distribution of the SHG signal, leading to nonlinear structured light generation.

We have tested these effects in the SHG response of isolated nanoribbons by scanning the pump light polarization relative to crystal orientation while detecting the SHG intensity with the same polarization. The SHG polarization response depends on the specific crystalline orientation of the nanoribbons, where two (for armchair) or four (for zigzag) lobes can be enhanced for the SHG component with polarization parallel to the pump beam. Both cases have been observed in our experiments and
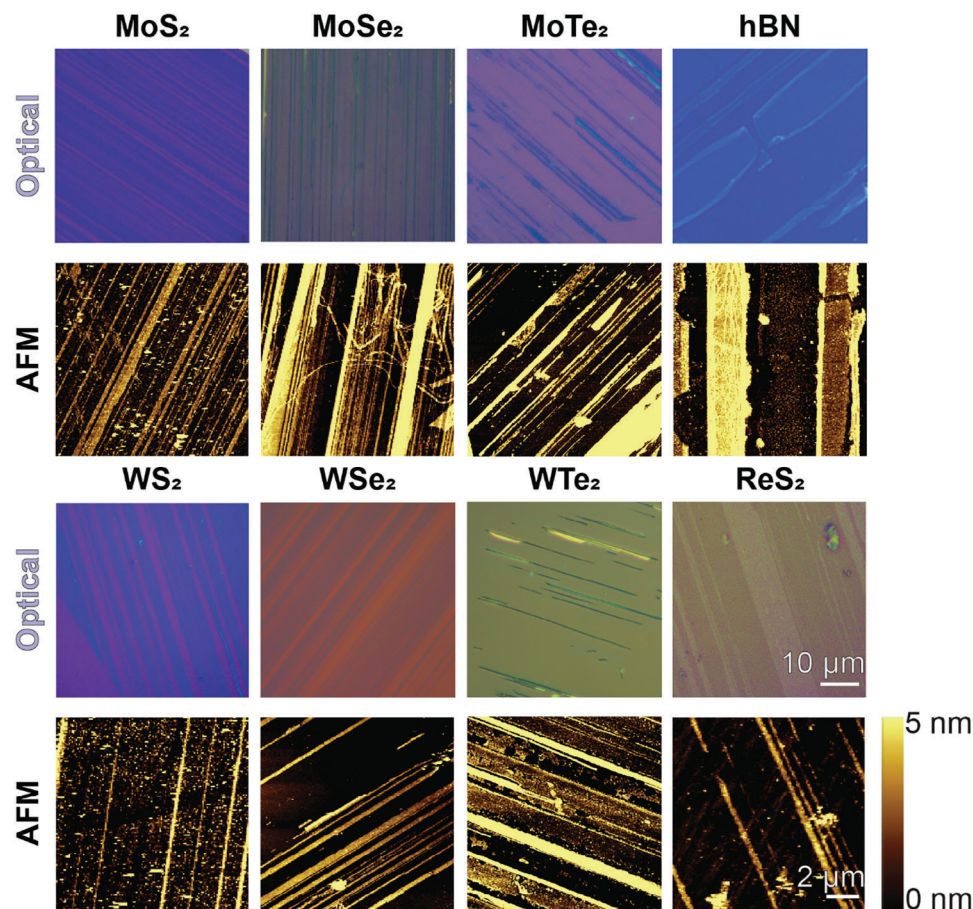
**ADVANCED
SCIENCE NEWS**

www.advancedsciencenews.com

NANO · MICRO

small

www.small-journal.com

Figure 2. Examples of exfoliated nanoribbons. Top, optical images and bottom, atomic force microscopy (AFM) images.

numerically simulated using COMSOL (Figure S4). Figure 3d shows a typical co-polarized SHG signal polarization scan measured from a 100 nm-wide nanoribbon along the armchair direction. It exhibits an asymmetrical SHG signal with an optical anisotropy of 22.6% between lobes along and away from the nanoribbon axis (purple circles in Figure 3d). This anisotropy agrees with the simulation results which predict a 35.6% anisotropy due to screening of the electric field (purple lines in Figure 3d). It is important to note that this anisotropy can be enhanced further by reducing the width of nanoribbons and additional effects contributing to anisotropy may arise from anisotropic strain within the ribbons.

3.2. Differential Doping Levels in Exfoliated MoS$_2$ Nanoribbons

Many vdW bulk crystals grow with zigzag edge termination due to their chemical stability over the armchair configuration.[35] As a result, our exfoliated nanoribbons are predominantly oriented along the zigzag direction. The outer edge of the ribbons maintains the geometry of the bulk crystal edges, while the inner edge is created from guided tearing where fracture of the monolayer follows the direction of the crystal step edges on top.[36] The crystal orientation of these nanoribbons was veri-

fied with SHG polarization scans (Figure 3d; Figure S4, Supporting Information). First principles calculations predict that TMDC nanoribbons with zigzag edges should exhibit ferromagnetic and metallic behavior,[8] with a magnetic moment that increases as the width increases so long as the ribbon remains at the nanoscale.[3] To identify if exfoliated nanoribbons are ferromagnetic, we performed magnetic force microscopy (MFM) measurements on MoS$_2$ nanoribbons. This two-pass AFM technique records topography and corresponding cantilever oscillation amplitude and phase at a lifted height, providing insight into the magnetic or electrostatic interaction forces exerted on the magnetic AFM probe.[37–40]

Figure 4 shows the MFM oscillation phase images of MoS$_2$ nanoribbons and larger area MoS$_2$ 2D flakes exfoliated from the same bulk crystal. The MFM phase shift, calculated by subtracting the response from the substrate, appears uniform across each nanoribbon as it reaches the limit of spatial resolution (Figure S5, Supporting Information). The edges on a 2D flake were slightly repulsive to the AFM probe, with a very small positive phase shift (Figure 4c). In contrast, for nanoribbons of various widths less than 300 nm, the phase shift of lifted cantilever oscillation is consistently more negative and therefore attractive (Figure 4d). A histogram demonstrating the phase shifts from multiple samples
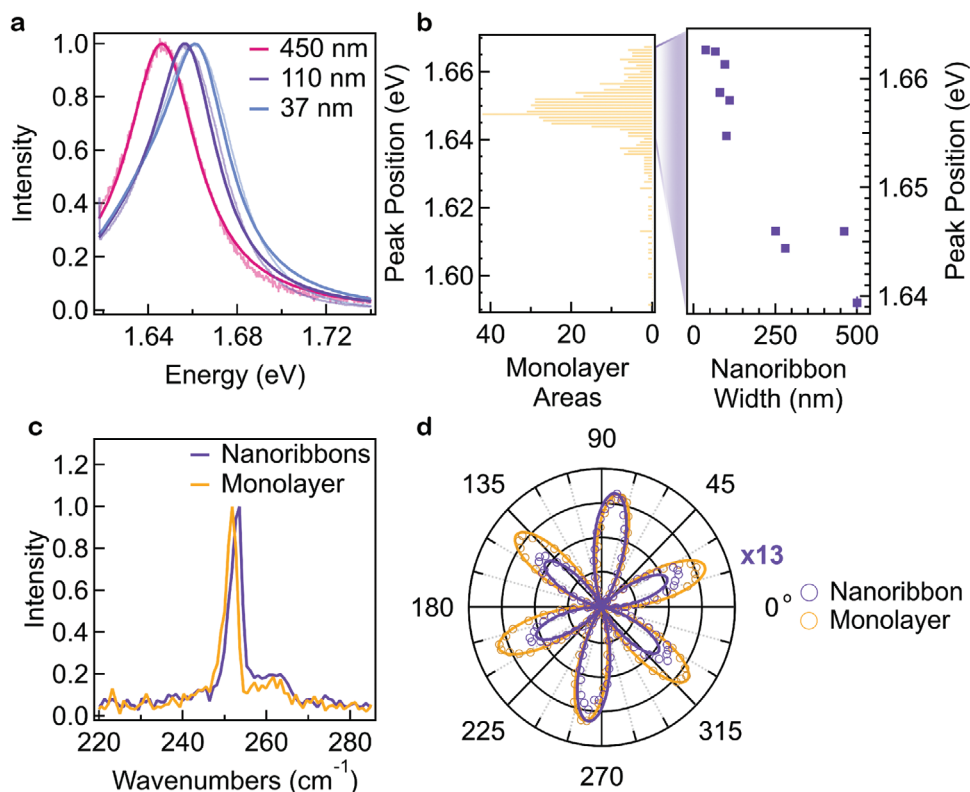
**ADVANCED
SCIENCE NEWS**

www.advancedsciencenews.com

**NANO · MICRO
small**

www.small-journal.com

Figure 3. Optical spectroscopy of WSe$_2$ nanoribbons. a) Photoluminescence spectra. The magenta, purple, and blue spectra correspond to nanoribbons of 450, 110, and 37 nm widths respectively. Widths were identified via AFM. The solid lines are Lorentzian fit functions. b) left, Distribution of PL emission peak wavelength for exfoliated WSe$_2$ monolayers; right, PL peak position of WSe$_2$ nanoribbons with different widths, exfoliated from the same crystal. Each point is the averaged signal from several spots along a ribbon spaced over at least 1 µm. c) Raman spectra for an area of nanoribbons (purple) compared with an unstrained monolayer area (gold). d) Normalized second harmonic generation intensity of radiation polarized parallel to a linearly polarized pump as a function of the pump polarization from a 100 nm WSe$_2$ nanoribbon oriented along the armchair direction (purple circles) in comparison to a WSe$_2$ monolayer (gold circles) and simulated anisotropy due to screening effects (lines). A nanoribbon oriented along the zigzag direction is shown in Figure S4.

is shown in Figure 4k. The negative phase is consistent among several ribbon samples, with wider nanoribbons exhibiting slightly stronger attraction than narrower ribbons.

To comprehensively assess the magnetic behavior, we conducted both reflective magnetic circular dichroism (RMCD), a microscope-based spatially resolved technique (Figure S7, Supporting Information), and vibrating sample magnetometry (VSM), a macroscopic characterization technique (Figure S8, Supporting Information). We do not observe ferromagnetism within individual exfoliated nanoribbons in RMCD. However, very weak ferromagnetic behavior is detected in VSM for densely packed nanoribbons and monolayers on a large scale. The macroscopic ferromagnetic responses can be influenced by multiple factors, such as metal vacancies,[41] chalcogen-metal antisites,[42,43] crystal edges, or grain boundaries,[41,42,44] as observed for weak ferromagnetism in large TMDC flakes and bulk crystals.[43,45–47] Indeed, when nanoribbons are grounded (Figure 4c), the strong attractive MFM phase disappears, indicating that the underlying mechanism of the attractive MFM response is an electrostatic interaction instead of a magnetic one. The presence of static charges may have arisen from chemical bond cleavage as the ribbons are torn from the bulk crystal during the exfoliation process.

To illustrate the microscopic electrostatic interaction, we conducted electrostatic force microscopy (EFM) on nanoribbons and 2D flakes exfoliated from the same crystal, using the same probe and lift height. In an EFM measurement, the tip oscillates above the sample while it is electrically biased. The measured phase shift of the tip reflects the electrostatic force gradient, which is related to the potential difference between the tip and the sample.[48] When a positive ($V_t = +1$ V) or negative ($V_t = -1$ V) bias is applied to the tip (Figure 4g–j), the EFM phase of the 2D flake is consistently negative. Similarly, the EFM phase in nanoribbons is negative at $V_t = +1$ V. However, when the bias is reversed ($V_t = -1$ V), the response dissipates at the center of the nanoribbons, while the negative phase response becomes more pronounced at the nanoribbon edges (Figure 4j). The different phase shifts under negative bias indicate that nanoribbon edges may have more p-doped character, which is consistent with the MoS$_2$ nanoribbons with bare sulfur terminated edges.[49] The nanoribbon body is more likely doped n-type, consistent with what is commonly found in TMDC monolayers with S vacancies. Similar characteristics can be observed in the amplitude signal (Figure S6, Supporting Information).
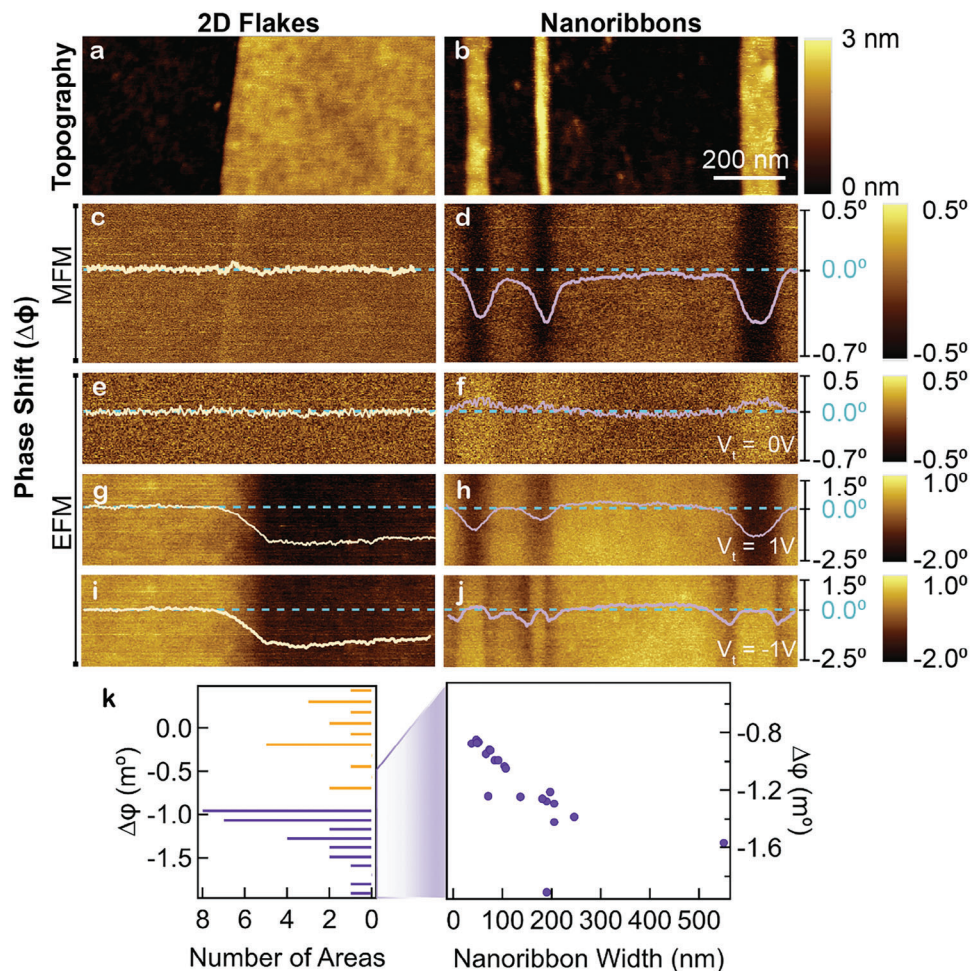
ADVANCED
SCIENCE NEWS
www.advancedsciencenews.com

NANO · MICRO
small
www.small-journal.com

Figure 4. Scanning Probe Microscopy of 2D MoS$_2$ flakes and MoS$_2$ nanoribbons. a,b) AFM topography images. c,d) Magnetic force microscopy oscillation phase images, with an overlayed profile of the MFM oscillation phase response and a zero-degree line (blue) for reference. e–j), Electrostatic force microscopy oscillation phase image at different tip voltages (V$_t$) (e,f) V$_t$ = 0 V, g,h) V$_t$ = +1 V, and i,j) V$_t$ = −1 V with an overlayed profile of the EFM oscillation phase response. k) left, Histogram comparing the MFM phase shift values among nanoribbons (purple) and edges of 2D flakes (gold), right, MFM oscillation phase of nanoribbons of differing widths. The 2D flakes and nanoribbons are exfoliated from the same crystal with similar thickness. All MFM/EFM measurements were carried out at 15 nm lift height, and phase traces subtract the phase response of the substrate.

3.3. Electrical Transport in Exfoliated MoS$_2$ Nanoribbons

We also evaluated the electrical properties of exfoliated, parallel aligned MoS$_2$ nanoribbons in fabricated devices with Au electrodes, as displayed in **Figure 5** (see Materials and Methods for fabrication and measurement details). Each device comprises several predominantly monolayer nanoribbons and multiple devices were measured with varying average nanoribbon widths (W$_{avg}$). The current density (I$_D$) through the nanoribbon devices was normalized by the totaled width of the nanoribbons. As the average ribbon width narrows, the minimum current measured (I$_{min}$) increases and the maximum current (I$_{max}$) decreases, causing the ratio of maximum-to-minimum current (I$_{max}$/I$_{min}$) to decrease, as shown in Figures 5b,c.

This trend suggests that the nanoribbon edges may be somewhat conductive, with increased I$_{min}$ through edges with partially zigzag (metallic)[3] character or from defect states in the

band gap. At high V$_{GS}$ (devices in the "on" state), the edge roughness could also play a greater role in narrower ribbons, consistent with previous observations of graphene and MoS$_2$ nanoribbons.[13,50] As a consequence, narrower ribbons tend to have higher contact resistance, as well as lower field-effect mobilities and I$_{max}$ (Figure S9, Supporting Information). The I$_{max}$/I$_{min}$ ratio for these nanoribbons reaches 10^4, which is comparable with that previously reported for monolayer MoS$_2$ nanoribbons created via lithography and select chemical vapor deposition growth,[11,13] as well as nanoribbons of bulk thickness created through plasma dry-etching and collapsed nanotubes.[11,51]

When a single narrow nanoribbon is isolated between two Au electrodes (Figure S9c, Supporting Information), its transfer characteristics display greater hysteresis between the forward and backward V$_{GS}$ sweeps, with a slight reduction in the I$_{max}$/I$_{min}$ ratio. This could be due to an increased influence of mid-gap edge defects and charge trappings from the surrounding

**ADVANCED
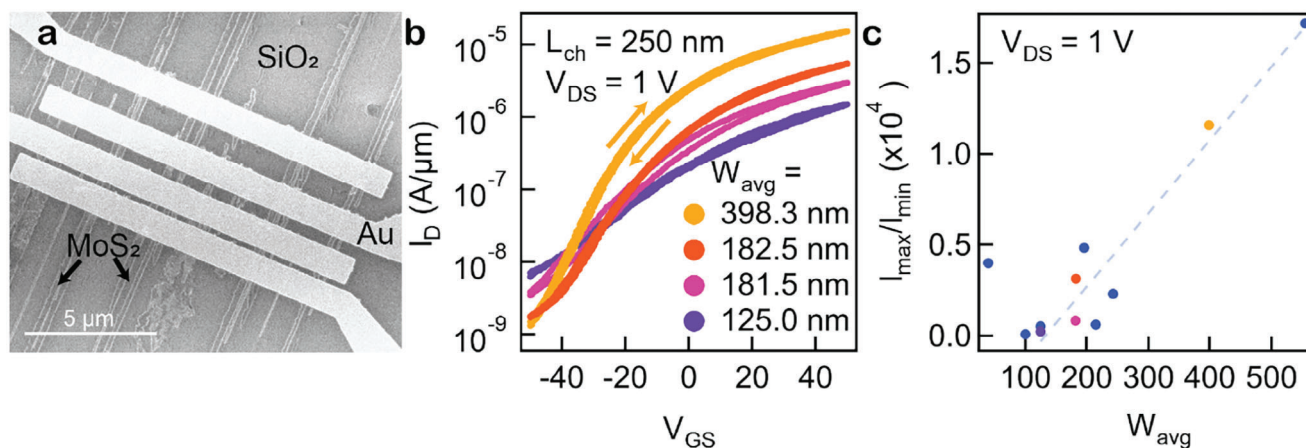SCIENCE NEWS**

www.advancedsciencenews.com

**NANO · MICRO
small**

www.small-journal.com

Figure 5. Electronic transport properties of MoS_2 nanoribbons. a) Top-down, scanning electron microscopy (SEM) image of parallel MoS_2 nanoribbons with Au contacts. The devices are on SiO_2 (90 nm) back-gated by the highly-doped Si below. b) Transfer characteristics of parallel nanoribbons with different average ribbon widths (W_{avg}) between electrodes. Small arrows on two curves of each kind mark the forward and backward V_{GS} sweeps,[58] revealing little hysteresis. c) On/off current (I_{max}/I_{min}) ratio for several devices with different average ribbon widths. The devices have a channel length (electrode separation) of 250 nm and $V_{DS} = 1$ V between the Au electrodes.

environment, without annealing or encapsulation with a dielectric layer. Compared to much wider monolayer devices,[52] the pronounced influence of edge properties from dielectric and chemical environments in nanoribbons could enable their applications in chemical sensing, electrocatalysis, and photocatalysis, and open up opportunities to explore and improve reaction mechanisms.

4. Conclusion

In this work, we introduced a versatile top-down exfoliation approach to obtain single crystal 2D nanoribbons directly from their corresponding bulk vdW crystals. The high-throughput approach facilitates the production of high-density, flat, and parallel-aligned nanoribbons from a diverse range of materials, covering large areas on various target substrates. Such capability is crucial for the extensive exploration of nanoribbons' distinct attributes through spectroscopic, imaging, and transport techniques. This top-down exfoliation method also offers a promise for versatile control of the nanoribbon morphology. Specifically, the nanoribbon width is determined by the polar cut angle θ, and the atomic alignment along the edge of the nanoribbons is determined by the azimuthal angle φ along the XY plane. If atomically flat crystal planes can be prepared with precisely controlled slant angles, such as using advanced controlled cross-section polishing techniques,[53,54] monodisperse nanoribbons with specifically tailored edge morphology and widths can be realized. Examples of such customization include TMDC nanoribbons with semiconducting armchair edges, conducting zigzag edges, or with particular cut directions in between the two geometries. This newfound accessibility to a broad variety of nanoribbon samples will unlock empirically observed properties expanding upon existing theoretical framework. It holds the potential to significantly contribute to a range of future technological applications for various nanoribbons, bridging the gap between theoretical predictions and practical implementation.

5. Experimental Section

Nanoribbon Exfoliation: TMDC crystals (HQ Graphene) and hBN crystals (2D Semiconductors) with exposed vicinal surfaces were deposited with a 100 nm thick layer of Au in an electron-beam evaporator (Kurt J. Lesker LAB18), at a deposition rate of 0.5 Å/s. The crystals coated with Au were then spin-coated with 10 wt.% polyvinyl pyrrolidone (Alfa Aesar) in 1:1 ethanol (Fisher Chemical) to acetonitrile (Fisher Chemical, >99.95%) at 400 rpm for two min. Next, a piece of thermal release tape (TRT, Semiconductor Equipment Corp., 90 °C release) was applied to the vicinal surface of the crystal covered in Au and PVP. The TRT was gently lifted, whilst keeping it flat, to remove the Au and top layer/layers of the crystal. The TRT/PVP/Au/nanoribbon stack was then placed, nanoribbon side down, onto the desired substrate (90 or 285 nm SiO_2 on Si, Nova Wafers). The stack was placed onto a hot plate at 100 °C to release the TRT. The PVP was then rinsed away thoroughly in DI water. The Au/nanoribbon/substrate stacks were then placed into a KI/I^- gold etchant (2.2 wt.% I_2 from Spectrum Chemical and 8.9 wt.% KI from Baker Chemical in DI water) for at least 4 min. Ultimately, samples were rinsed in DI water, then isopropanol (Fisher Chemical, >99.5), and promptly dried with a N_2 gun.

Photoluminescence and Raman Spectroscopy: Photoluminescence and Raman spectra were taken at room temperature inside a home-built nitrogen cell using a home-built optical spectroscopy setup. A 532 nm cw laser (CNI laser, at 33 µW for PL and 110 µW for Raman spectroscopy) was focused on the nanoribbons to the diffraction limit with a 150 X objective (Nikon Confocal Plan Apochromat). The emitted light from the nanoribbon passes through a 550 nm long-pass filter (Thorlabs) for PL and volume Bragg gratings (OptiGRATE) for Raman spectroscopy measurements. The photoluminescence and Raman spectra were collected with a spectrograph (Princeton Instruments, HRS-300-S) and a camera (Princeton Instruments, PIX-400BR). To extract central wavelength, peaks in the recorded spectra were fit with Lorentzian functions.

Second Harmonic Generation (SHG): Optical second harmonic generation measurements were performed using 1030-nm pump pulses from a femtosecond laser (NKT Origami Onefive 10, pulse duration < 200 fs). The pump pulses were focused on the sample, held under N_2, at normal incidence with a 40 X Nikon Plan Fluor objective. The reflected pump and SH beams were separated using a dichroic mirror and the SH signal was recorded, after passing through a short-pass filter, by an EM CCD (Andor iXon Ultra). Both the incident pump and reflected SH beams passed through a rotating half waveplate. This produces an SH response from TMDC samples with sixfold symmetry as a function of rotation of the half

**ADVANCED
SCIENCE NEWS**

www.advancedsciencenews.com

**NANO · MICRO
small**

www.small-journal.com

waveplate, equivalent to the effect of rotating the sample about its surface normal.

Numerical Simulations: We performed 2D finite-element simulations in the frequency domain to model the optical respone of monolayer WSe_2 nanoribbons on a 90 nm-thick SiO_2 on Si substrate using the commercial software package COMSOL (COMSOL, Inc.). The simulation area was defined as a 2 μm-sized box surrounded by a 200 nm-thick perfect matching layer. Each nanoribbon was modeled as a 0.649 nm-thick dielectric slab illuminated by a plane wave at the pump wavelength of 1030 nm to extract the external optical anisotropy at the fundamental frequency. The induced nonlinear source polarization was then calculated analytically by considering the nonlinear susceptibility tensor of an ideal, infinite WSe_2 monolayer. The response was determined by the input polarization as well as the angle between the crystal axes and the ribbon orientation. We then simulated the resulting radiation at the second-harmonic frequency using the COMSOL package. To compare with the experimental results, we integrated the Poynting vector for the component of the second-harmonic radiation parallel to the pump beam within a fixed range of solid angles. The dispersion of the WSe_2 monolayer was taken into account, and the refractive indices of SiO_2 and Si were set as 1.45 and 3.54, respectively.

Reflection Magnetic Circular Dichroism (RMCD): RMCD signal was measured with the sample loaded in an Attocube attoDRY2100 cryostat, which could apply up to a 9 T magnetic field. The optical path design follows that of Huang, et al.[55] and Sato[56] in which a photo-elastic modulator was employed to produce states of oscillating circularly polarized light. Measurements were made at 532 nm with a Coherent Verdi V5 laser. This probe beam was chopped at 137 Hz with linear polarization at 45° to the fast axis of photo-elastic modulator (PEM, Hind Instruments, PEM series I). The PEM had 50 kHz sinusoidal retardation, with a maximum quarter-wave to produce LCP and RCP light. The probe light, after reflection from the sample, was collected by a photodiode (Thorlabs, DET36A). Lock-in amplifiers were used to obtain signals at the chopper frequency and PEM frequency, from which the reflectivity difference (RMCD percentage) was determined.[56]

Atomic Force Microscopy: Topography images of nanoribbon and monolayer samples were collected at room temperature with Atomic Force Microscopy (Park Systems, Park NX-10, Park XE-70, or XE-100) and a MikroMasch HQ:NSC15/Al BS probe. All Magnetic Force Microscopy and Electrostatic Force Microscopy measurements were taken using a Park NX-10 and a Nanosensors PPP-LC-MFMR probe at a 15 nm lift height above the sample surface. Topography and MFM/EFM phase profiles were obtained from averaging line scans over 32 nm of 1×1 μm images.

Electrical Measurements: To characterize the electrical transport properties, field-effect transistors were fabricated on 90 nm SiO_2 on p^{++} Si substrates, which also served as the back-gate. The larger contact pads and leads were patterned with electron-beam (e-beam) lithography using PMMA (polymethyl methacrylate) as the resist. Large contact pads and leads consist of an e-beam evaporated stack with 25 nm SiO_2, 3 nm Ti, and 40 nm Au. The SiO_2 layer reduces the leakage from the large contact pads to the substrate, and the Ti layer improves the adhesion of the Au. The finer leads, which make direct contact with the MoS_2, were similarly patterned with e-beam lithography and consist of 40 nm of pure Au deposited with e-beam evaporation at low pressure (10^{-7} Torr or lower).[57] Lift-off of the contacts and pads was done in room temperature acetone. These devices were measured under vacuum ($<10^{-5}$ Torr) at room temperature in a Janis ST-100 probe station with a Keithley 4200 Semiconductor Characterization System.

Supporting Information

Supporting Information is available from the Wiley Online Library or from the author.

Conflict of Interest

The authors declare no conflict of interest.

Author Contributions

F.L. conceived the work. A.P.S. performed exfoliations, and all optical imaging and AFM-based characterizations apart from the exfoliation of hBN (performed by A.M.G.), the exfoliation of $MoTe_2$ (performed by H.J.Z), and the exfoliation and topographical image of ReS_2 (performed by A.C.J). A.P.S. carried out all photoluminescence spectroscopy, Raman spectroscopy, and second harmonic generation characterizations. V.C. performed device fabrication and electrical transport analysis, with advice from E.P. J.W. collected RMCD and aided A.P.S. in analysis of results. T.T. and T.K.M performed all VSM measurements and analysis. Q.L. carried out the analysis and simulation of optical anisotropy effects in the SHG response. A.P.S. and F.L. wrote this manuscript with input from all authors, and all authors contributed to the discussion and interpretation of the data presented in this work.

Data Availability Statement

The data that support the findings of this study are available from the corresponding author upon reasonable request.

Keywords

2D materials, doping, exfoliation methods, scanning probe microscopy

[1] K. S. Novoselov, A. K. Geim, S. V. Morozov, D. Jiang, Y. Zhang, S. V. Dubonos, I. V. Grigorieva, A. A. Firsov, *Science* **2004**, *306*, 666.

[2] A. P. Alivisatos, *Science* **1996**, *271*, 933.

[3] Y. Li, Z. Zhou, S. Zhang, Z. Chen, *J. Am. Chem. Soc.* **2008**, *130*, 16739.

[4] X. Wu, X. Zhang, X. Wang, Z. Zeng, *AIP Adv.* **2016**, *6*, 45318.

[5] F. Shayeganfa, A. Ramazani, H. Habibiyan, *Sci. Rep.* **2024**, *14*, 1581.

[6] H. Zeng, C. Zhi, Z. Zhang, X. Wei, X. Wang, W. Guo, Y. Bando, D. Golberg, *Nano Lett.* **2010**, *10*, 5049.

[7] A. Lopez-Bezanilla, J. Huang, H. Terrones, B. G. Sumpter, *Nano Lett.* **2011**, *11*, 3267.

[8] D. Davelou, G. Kopidakis, E. Kaxiras, I. N. Remediakis, *Phys. Rev. B* **2017**, *96*, 165436.

[9] H. Zhang, X.-B. Li, L.-M. Liu, *J. Appl. Phys.* **2013**, *114*, 093710.

[10] D. Kotekar-Patil, J. Deng, S. L. Wong, C. S. Lau, K. E. J. Goh, *Appl. Phys. Lett.* **2019**, *114*, 13508.

[11] H. Liu, J. Gu, P. D. Ye, *IEEE Electron Device Lett.* **2012**, *33*, 1273.

[12] Y. Deng, C. Zhu, Y. Wang, X. Wang, X. Zhao, Y. Wu, B. Tang, R. Duan, K. Zhou, Z. Liu, *Mater. Today* **2022**, *58*, 8.

[13] S. Chen, S. Kim, W. Chen, J. Yuan, R. Bashir, J. Lou, A. M. van der Zande, W. P. King, *Nano Lett.* **2019**, *19*, 2092.

[14] J. Wu, H. Zhao, Y. Li, D. Ohlberg, W. Shi, W. Wu, H. Wang, P. Tan, *Adv. Opt. Mater.* **2016**, *4*, 756.

[15] D. S. Fox, Y. Zhou, P. Maguire, A. Oneill, C. Ócoileaín, R. Gatensby, A. M. Glushenkov, T. Tao, G. S. Duesberg, I. V. Shvets, M. Abid, M. Abid, H. C. Wu, Y. Chen, J. N. Coleman, J. F. Donegan, H. Zhang, *Nano Lett.* **2015**, *15*, 5307.

[16] M. C. Watts, L. Picco, F. S. Russell-Pavier, P. L. Cullen, T. S. Miller, S. P. Bartuś, O. D. Payton, N. T. Skipper, V. Tileli, C. A. Howard, *Nature* **2019**, *568*, 216.

[17] Z. Wang, X. Zhang, J. A. Hachtel, A. Apte, C. S. Tiwary, R. Vajtai, J. C. Idrobo, R. Ozturk, P. Ajayan, *Nanoscale Horiz.* **2019**, *4*, 689.

[18] Y. Chen, P. Cui, X. Ren, C. Zhang, C. Jin, Z. Zhang, C.-K. Shih, *Nat. Commun.* **2017**, *8*, 15135.

[19] S. M. Poh, S. J. R. Tan, X. Zhao, Z. Chen, I. Abdelwahab, D. Fu, H. Xu, Y. Bao, W. Zhou, K. P. Loh, *Adv. Mater.* **2017**, *29*, 1605641.

[20] Z. Wang, H. Li, Z. Liu, Z. Shi, J. Lu, K. Suenaga, S. K. Joung, T. Okazaki, Z. Gu, J. Zhou, Z. Gao, G. Li, S. Sanvito, E. Wang, S. Iijima, *J. Am. Chem. Soc.* **2010**, *132*, 13840.

[21] T. Chowdhury, J. Kim, E. C. Sadler, C. Li, S. W. Lee, K. Jo, W. Xu, D. H. Gracias, N. V. Drichko, D. Jariwala, T. H. Brintlinger, T. Mueller, H.-G. Park, T. J. Kempa, *Nat. Nanotechnol.* **2020**, *15*, 29.

[22] E. C. Sadler, T. Chowdhury, R. Dziobek-Garrett, C. Li, O. Ambrozaite, T. Mueller, T. J. Kempa, *ACS Appl. Nano Mater.* **2022**, *5*, 11423.

[23] A. Aljarb, J.-H. Fu, C.-C. Hsu, C.-P. Chuu, Y. Wan, M. Hakami, D. R. Naphade, E. Yengel, C.-J. Lee, S. Brems, T.-A. Chen, M.-Y. Li, S.-H. Bae, W.-T. Hsu, Z. Cao, R. Albaridy, S. Lopatin, W.-H. Chang, T. D. Anthopoulos, J. Kim, L.-J. Li, V. Tung, *Nat. Mater.* **2020**, *19*, 1300.

[24] P. Yang, D. Wang, X. Zhao, W. Quan, Q. Jiang, X. Li, B. Tang, J. Hu, L. Zhu, S. Pan, Y. Shi, Y. Huan, F. Cui, S. Qiao, Q. Chen, Z. Liu, X. Zou, Y. Zhang, *Nat. Commun.* **2022**, *13*, 3238.

[25] F. Cheng, H. Xu, W. Xu, P. Zhou, J. Martin, K. P. Loh, *Nano Lett.* **2017**, *17*, 1116.

[26] S. Li, Y. C. Lin, W. Zhao, J. Wu, Z. Wang, Z. Hu, Y. Shen, D. M. Tang, J. Wang, Q. Zhang, H. Zhu, L. Chu, W. Zhao, C. Liu, Z. Sun, T. Taniguchi, M. Osada, W. Chen, Q. H. Xu, A. T. S. Wee, K. Suenaga, F. Ding, G. Eda, *Nat. Mater.* **2018**, *17*, 535.

[27] P. Walker, W. H. Tarn, *CRC Handbook of Metal Etchants*, CRC Press LLC, Boca Raton, Florida, **1991**.

[28] F. Liu, W. Wu, Y. Bai, S. H. Chae, Q. Li, J. Wang, J. Hone, X.-Y. Zhu, *Science* **2020**, *367*, 903.

[29] S. B. Desai, S. R. Madhvapathy, M. Amani, D. Kiriya, M. Hettick, M. Tosun, Y. Zhou, M. Dubey, J. W. Ager, D. Chrzan, A. Javey, *Adv. Mater.* **2016**, *28*, 4053.

[30] M. Velický, G. E. Donnelly, W. R. Hendren, S. McFarland, D. Scullion, W. J. I. DeBenedetti, G. C. Correa, Y. Han, A. J. Wain, M. A. Hines, D. A. Muller, K. S. Novoselov, H. D. Abruña, R. M. Bowman, E. J. G. Santos, F. Huang, *ACS Nano* **2018**, *12*, 10463.

[31] Y. Huang, Y.-H. Pan, R. Yang, L.-H. Bao, L. Meng, H.-L. Luo, Y.-Q. Cai, G.-D. Liu, W.-J. Zhao, Z. Zhou, L.-M. Wu, Z.-L. Zhu, M. Huang, L.-W. Liu, L. Liu, P. Cheng, K.-H. Wu, S.-B. Tian, C.-Z. Gu, Y.-G. Shi, Y.-F. Guo, Z. G. Cheng, J.-P. Hu, L. Zhao, G.-H. Yang, E. Sutter, P. Sutter, Y.-L. Wang, W. Ji, X.-J. Zhou, et al., *Nat. Commun.* **2020**, *11*, 2453.

[32] R. Canton-Vitoria, T. Hotta, M. Xue, S. Zhang, R. Kitaura, *JACS Au* **2022**, *3*, 775.

[33] T. P. Darlington, C. Carmesin, M. Florian, E. Yanev, O. Ajayi, J. Ardelean, D. A. Rhodes, A. Ghiotto, A. Krayev, K. Watanabe, T. Taniguchi, J. W. Kysar, A. N. Pasupathy, J. C. Hone, F. Jahnke, N. J. Borys, P. J. Schuck, *Nat. Nanotechnol.* **2020**, *15*, 854.

[34] A. M. Dadgar, D. Scullion, K. Kang, D. Esposito, E. H. Yang, I. P. Herman, M. A. Pimenta, E. J. G. Santos, A. N. Pasupathy, *Chem. Mater.* **2018**, *30*, 5148.

[35] W. Fu, M. John, T. D. Maddumapatabandi, F. Bussolotti, Y. S. Yau, M. Lin, K. E. Johnson Goh, *ACS Nano* **2023**, *17*, 16348.

[36] A. Ibarra, J. F. Fuentealba, J. Bico, B. Roman, F. Melo, *Phys. Rev. Mater.* **2021**, *5*, 25601.

[37] Y. Martin, H. K. Wickramasinghe, *Appl. Phys. Lett.* **1987**, *50*, 1455.

[38] D. Rugar, H. J. Mamin, P. Guethner, S. E. Lambert, J. E. Stern, I. McFadyen, T. Yogi, *J. Appl. Phys.* **1990**, *68*, 1169.

[39] U. Hartmann, T. Göddenhenrich, C. Heiden, *J. Magn. Magn. Mater.* **1991**, *101*, 263.

[40] T. Thomson, in *Metallic Films for Electronic, Optical and Magnetic Applications* (Eds.: K. Barmak, K. Coffey), Elsevier, Amsterdam, Netherlands **2014**, pp. 454–546.

[41] A. A. Koós, P. Vancsó, M. Szendrö, G. Dobrik, D. Antognini Silva, Z. I. Popov, P. B. Sorokin, L. Henrard, C. Hwang, L. P. Biró, L. Tapasztó, *J. Phys. Chem. C* **2019**, *123*, 24855.

[42] N. Gao, Y. Guo, S. Zhou, Y. Bai, J. Zhao, *J. Phys. Chem. C* **2017**, *121*, 12261.

[43] Z. Guguchia, A. Kerelsky, D. Edelberg, S. Banerjee, F. von Rohr, D. Scullion, M. Augustin, M. Scully, D. A. Rhodes, Z. Shermadini, H. Luetkens, A. Shengelaya, C. Baines, E. Morenzoni, A. Amato, J. C. Hone, R. Khasanov, S. J. L. Billinge, E. Santos, A. N. Pasupathy, Y. J. Uemura, *Sci. Adv.* **2018**, *4*, aat3672.

[44] A. R. Botello-Méndez, F. López-Urías, M. Terrones, H. Terrones, *Nanotechnology* **2009**, *20*, 325703.

[45] D. Gao, M. Si, J. Li, J. Zhang, Z. Zhang, Z. Yang, D. Xue, *Nanoscale Res. Lett.* **2013**, *8*, 129.

[46] X. Mao, X. Xu, Q. Xue, W. Wang, D. Gao, *Nanoscale Res. Lett.* **2013**, *8*, 430.

[47] H. Li, X. Qi, J. Wu, Z. Zeng, J. Wei, H. Zhang, *ACS Nano* **2013**, *7*, 2842.

[48] C. H. Lei, A. Das, M. Elliott, J. E. Macdonald, *Nanotechnology* **2004**, *15*, 627.

[49] M. Gibertini, N. Marzari, *Nano Lett.* **2015**, *15*, 6229.

[50] A. Behnam, A. S. Lyons, M. H. Bae, E. K. Chow, S. Islam, C. M. Neumann, E. Pop, *Nano Lett.* **2012**, *12*, 4424.

[51] S. Fathipour, M. Remskar, A. Varlec, A. Ajoy, R. Yan, S. Vishwanath, S. Rouvimov, W. S. Hwang, H. G. Xing, D. Jena, A. Seabaugh, *Appl. Phys. Lett.* **2015**, *106*, 022114.

[52] C. J. McClellan, E. Yalon, K. K. H. Smithe, S. V. Suryavanshi, E. Pop, *ACS Nano* **2021**, *15*, 1587.

[53] J. Benedict, R. Anderson, S. J. Klepeis, *MRS Proc.* **1991**, *254*, 121.

[54] R. Jiang, M. Li, Y. Yao, J. Guan, H. Lu, *Front. Mater. Sci.* **2019**, *13*, 107.

[55] B. Huang, G. Clark, E. Navarro-Moratalla, D. R. Klein, R. Cheng, K. L. Seyler, D. i. Zhong, E. Schmidgall, M. A. McGuire, D. H. Cobden, W. Yao, D. Xiao, P. Jarillo-Herrero, X. Xu, *Nature* **2017**, *546*, 270.

[56] K. Sato, *Jpn. J. Appl. Phys.* **1981**, *20*, 2403.

[57] C. D. English, G. Shine, V. E. Dorgan, K. C. Saraswat, E. Pop, *Nano Lett.* **2016**, *16*, 3824.

[58] Z. Cheng, C.-S. Pang, P. Wang, S. T. Le, Y. Wu, D. Shahrjerdi, I. Radu, M. C. Lemme, L.-M. Peng, X. Duan, Z. Chen, J. Appenzeller, S. J. Koester, E. Pop, A. D. Franklin, C. A. Richter, *Nat. Electron.* **2022**, *5*, 416.

Supporting Information

Direct Exfoliation of Nanoribbons from Bulk van der Waals Crystals

Ashley P. Saunders, Victoria Chen, Jierong Wang, Qitong Li, Amalya C. Johnson, Amy S. McKeown-Green, Helen J. Zeng, T. Kien Mac, M. Tuan Trinh, Tony F. Heinz, Eric Pop, Fang Liu*
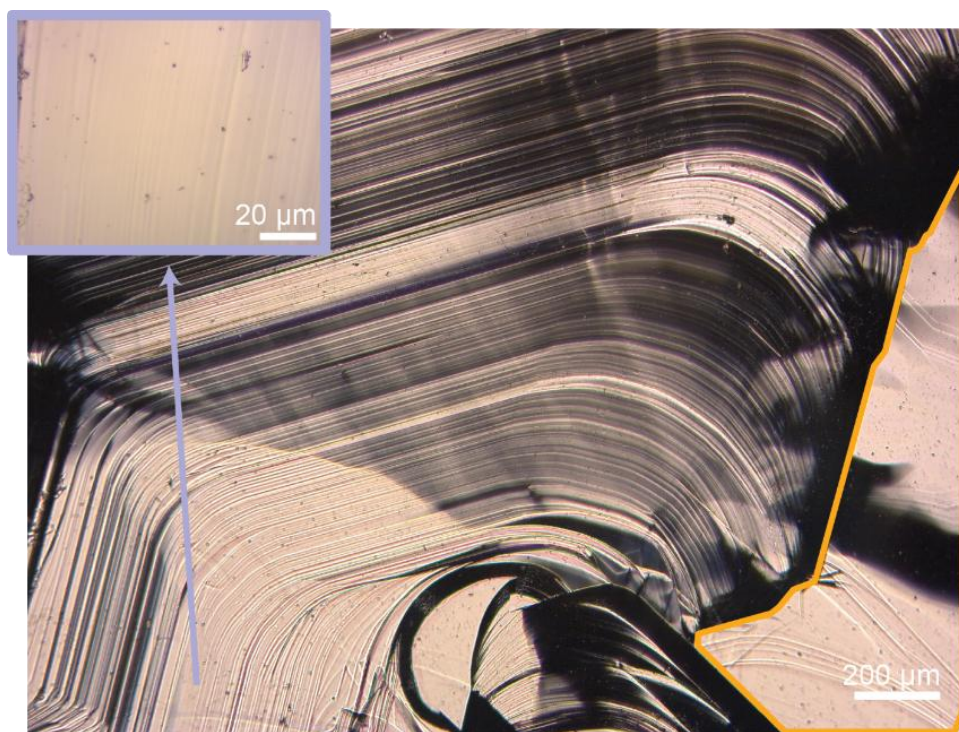
Figure S1. Optical Image of exemplary surfaces on a bulk MoS_2 crystal. Exfoliation from the vicinal surface (blue) and a flat area (gold) shown in the optical image leads to production of nanoribbons and monolayers respectively.
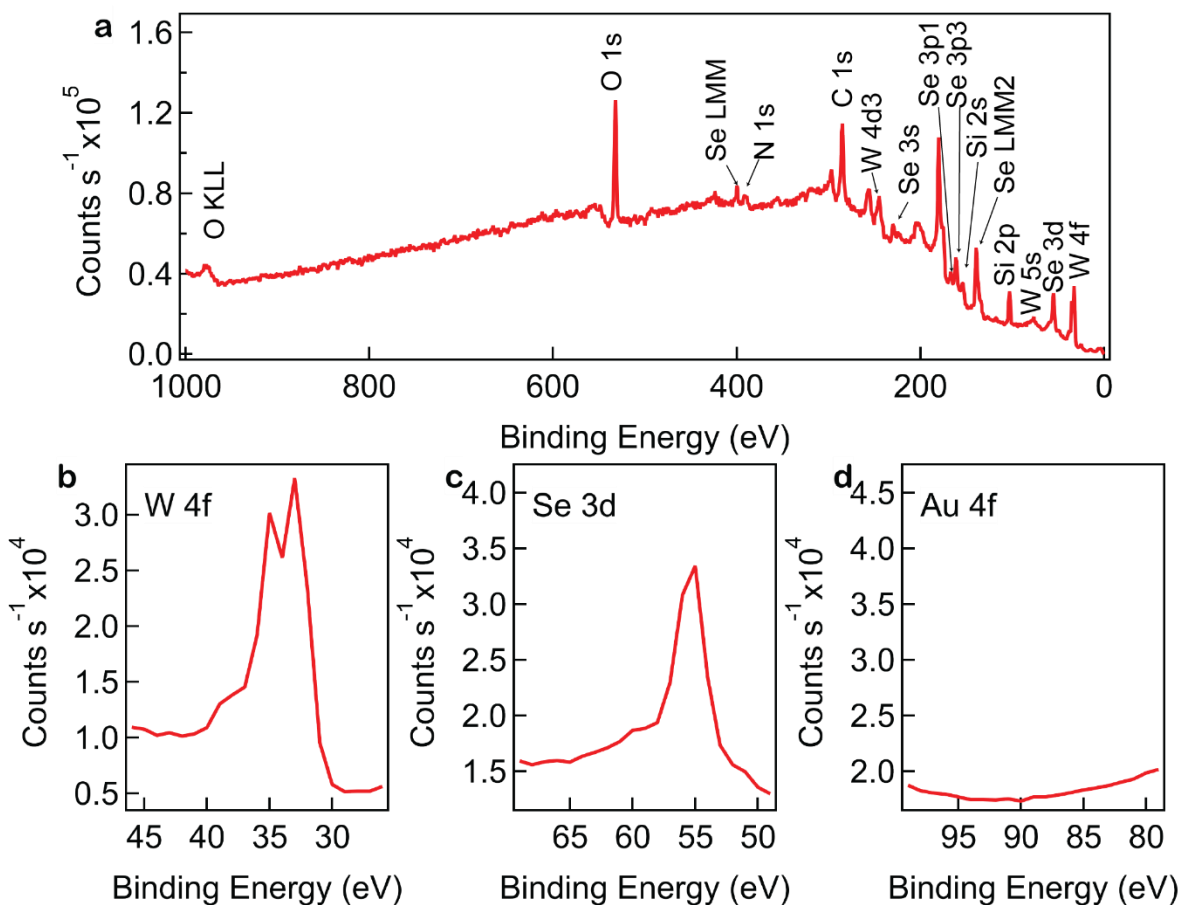
Figure S2. X-ray photoemission spectroscopy (XPS) on a macroscopic area of WSe_2 monolayer nanoribbons exfoliated on 285 nm SiO_2/Si. (a) Broad survey from 0 – 1100 eV. (b – d) Fine spectra of W, Se, and Au respectively, displaying clean removal of Au. All XPS measurements were taken with a PHI VersaProbe 3 at room temperature.
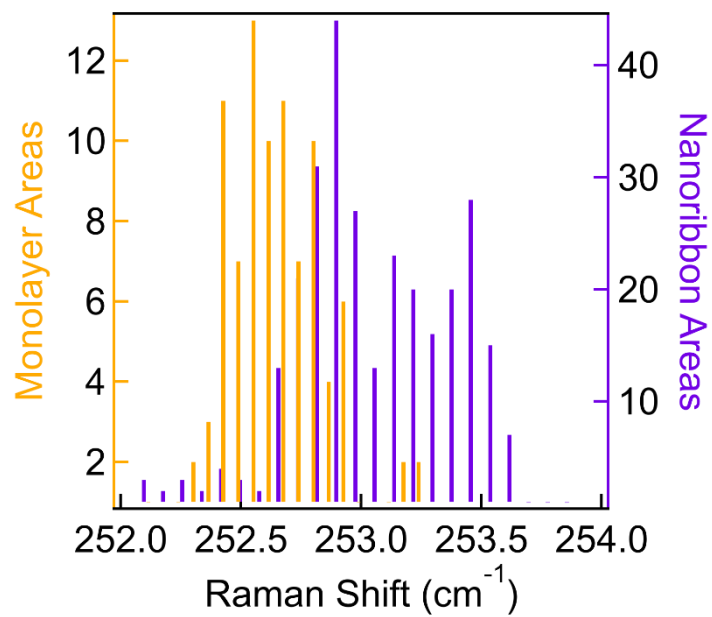
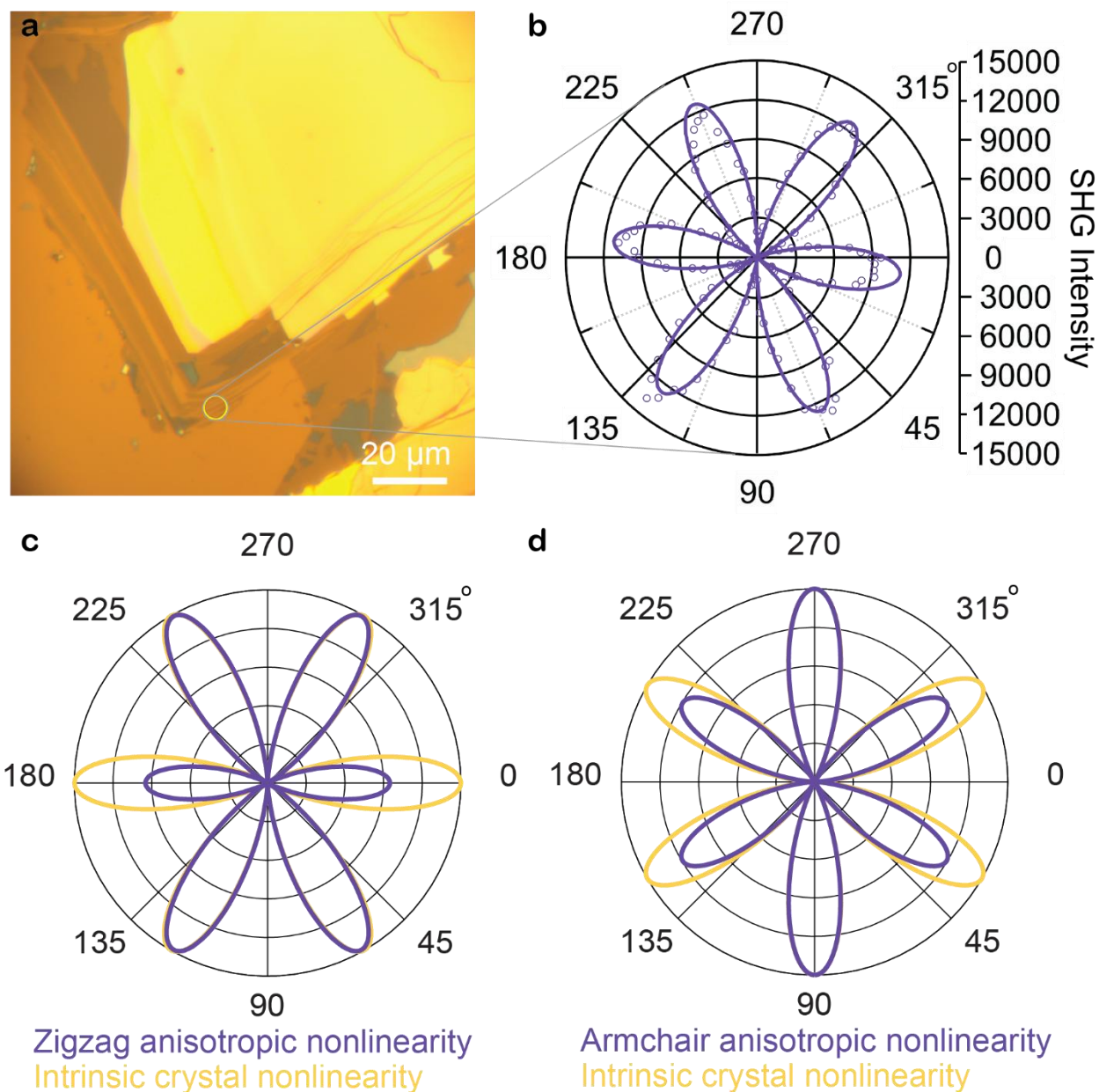**Figure S3.** Distribution of E′ peak position in Raman spectroscopy of WSe$_2$ monolayer (gold) and nanoribbons (purple) ranging from 20 to 400 nm wide.

Figure S4. Determination of Crystal Orientation. (a) Optical image of WSe$_2$ nanoribbons oriented along the zigzag direction. (b) Second Harmonic Generation (SHG) polarization scan for a 500 nm-wide WSe$_2$ nanoribbon oriented along the zigzag direction (purple circles) with overlayed simulated anisotropic nonlinearity (purple line). (c,d) Simulated second harmonic generation polarization scans for 100 nm-wide WSe$_2$ nanoribbons, showing the anisotropic nonlinearity for a nanoribbons with edges oriented along the zigzag and armchair axes respectively (purple lines), in comparison to the intrinsic crystal nonlinearity (gold).
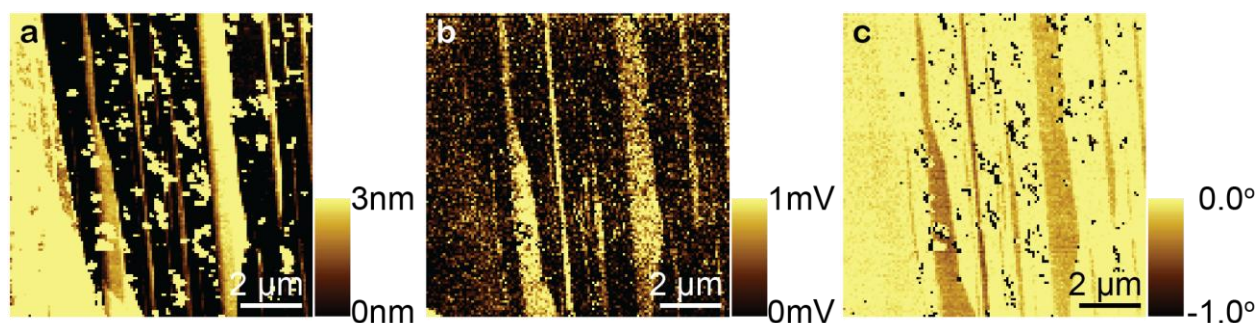
Figure S5. Magnetic Force Microscopy on a large area of MoS₂ nanoribbons of different width. (a) AFM topography image with nanoribbons colored brown and the SiO₂ substrate in black. The bright yellow spots are residual carbide contamination from the crystal growth process. (b) MFM amplitude. (c) MFM phase. These scans were taken at a 15 nm lift height.
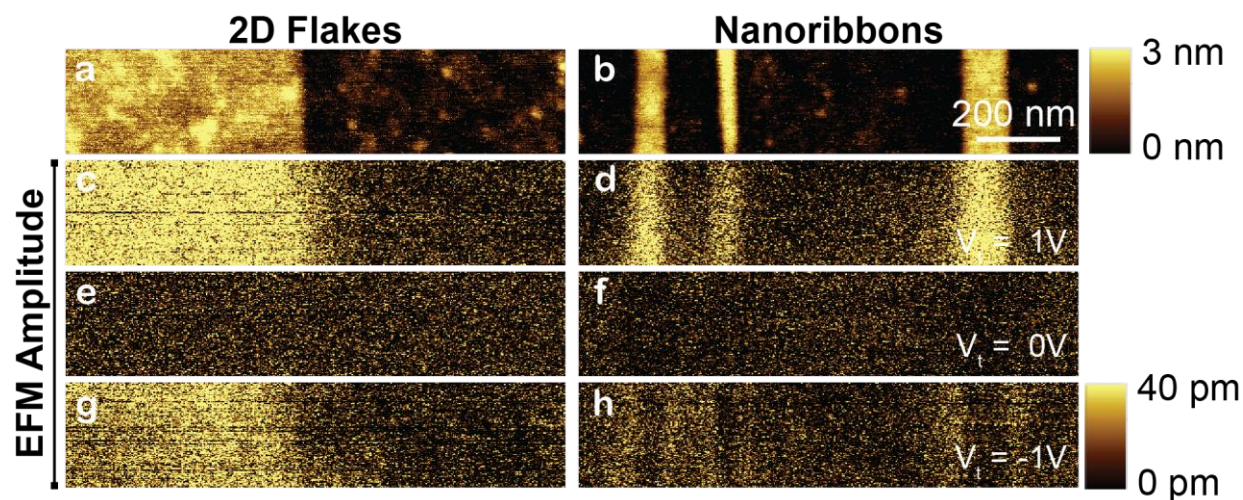

Figure S6. Electrostatic Force Microscopy Amplitude of 2D MoS₂ flakes and nanoribbons. (a,b) AFM topography images. (c – h) Electrostatic force microscopy amplitude image of the same respective area of the 2D flake or nanoribbons at different tip biases (V_t): (c, d) $V_t = +1$ V, (e, f) $V_t = 0$ V, and (g, h) $V_t = -1$ V.
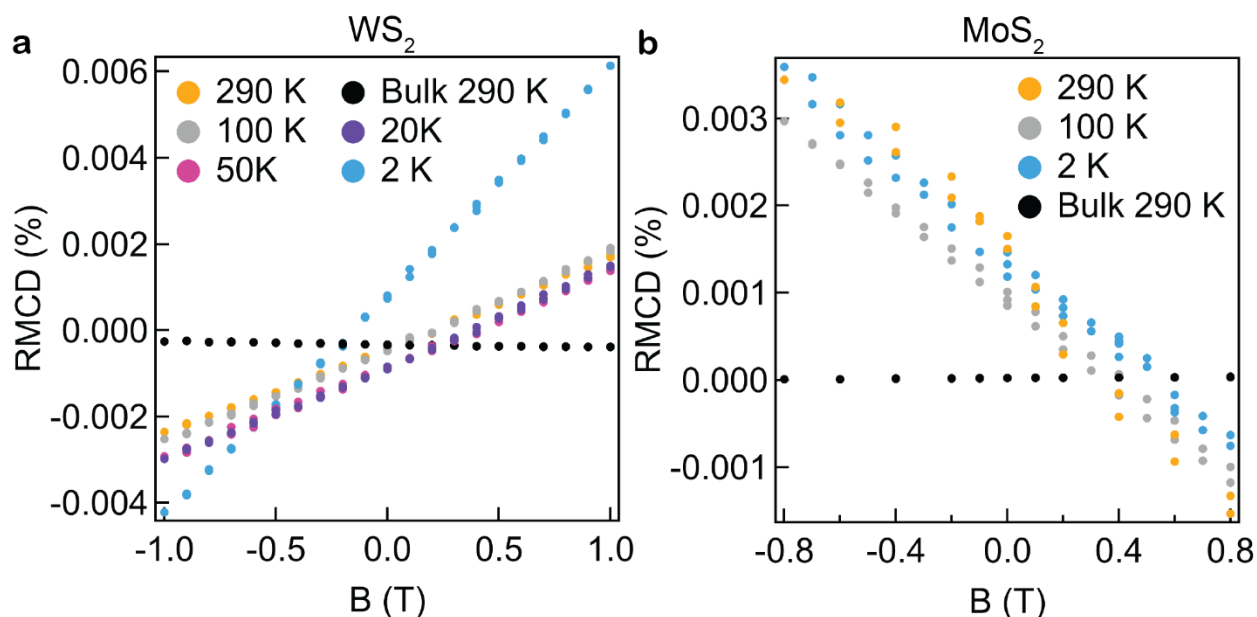
Figure S7. Reflection Magnetic Circular Dichroism (RMCD) response of TMDC nanoribbons. (a) RMCD spectra probing the edge of a 390 nm wide WS_2 nanoribbon supported on a 90 nm SiO_2/Si substrate at various temperatures: 2 K (blue), 20 K (purple), 50 K (magenta), 100 K (gray), and 290 K (gold) in comparison to the flat surface of bulk WS_2 at 290 K (black). The positive slope of the temperature dependent RMCD indicates a weak paramagnetic response in WS_2 nanoribbons in comparison to the bulk. (b) RMCD spectra probing an area of MoS_2 nanoribbons that are less than 150 nm wide supported on a 90 nm SiO_2/Si substrate at various temperatures: 2 K (blue), 100 K (gray), and 290 K (gold) in comparison to bulk MoS_2 (black). The lack of hysteresis in the RMCD is compatible with non-ferromagnetic behavior in the nanoribbons.
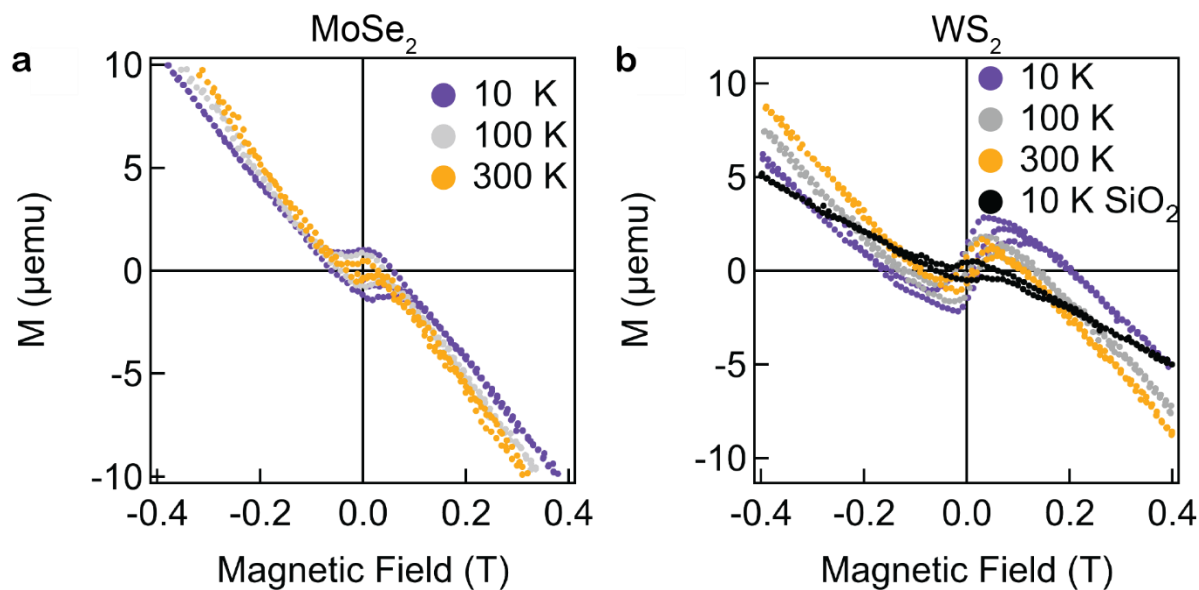
Figure S8. Vibrating Sample Magnetometry (VSM). (a) Magnetization of MoSe$_2$ nanoribbons on 285 nm SiO$_2$/Si as a function of applied magnetic field at 10 K (purple), 100 K (gray), and 300 K (gold). (b) VSM signal from WS$_2$ on 285 nm SiO$_2$/Si at 10 K (purple), 100 K (gray), and 300 K (gold), and a bare 285 nm SiO$_2$/Si substrate at 10 K (black). These results on samples with a high density of WS$_2$ and MoSe$_2$ nanoribbons reveal very weak ferromagnetic responses at the macroscopic scale, with the coercivity of WS$_2$ nanoribbons being comparable to that observed in sonicated WS$_2$ nanosheets.[46] This could be an effect from multiple factors, such as metal vacancies, chalcogen-metal antisites, crystal edges, or the remaining bulk pieces on the substrate.
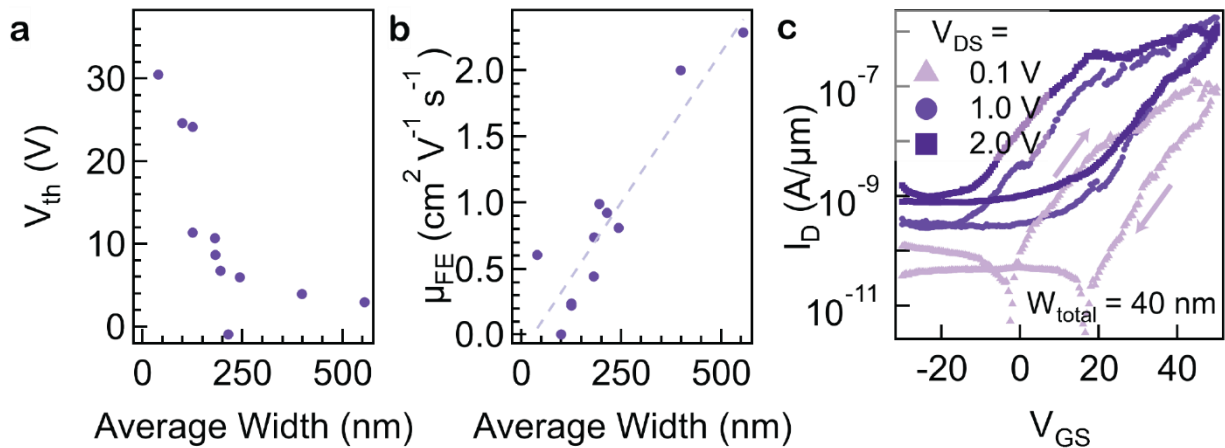
Figure S9. Auxiliary transport characteristics for MoS$_2$ nanoribbon field effect transistors. (a) Threshold voltage, estimated by linear extrapolation at maximum transconductance, as a function of average nanoribbon width. Threshold voltages were averaged between the forward and backward sweeps due to increased hysteresis. This shows a trend of increasing V_{th} as the channels become narrower, similar to that previously seen for MoS$_2$ channels narrowed through plasma dry etching.[2] (b) Field-effect electron mobility versus average nanoribbon width. The trend of decreasing mobility at narrower channel widths is in agreement with that seen in MoS$_2$ nanoribbons fabricated by scanning probe lithography.[3] (c) Measured transfer characteristics of an isolated 40 nm wide nanoribbon, with different V_{DS}. Small arrows mark the forward and backward V_{GS} sweeps.

References

[1]   X. Mao, Y. Xu, Q. Xue, W. Wang, D. Gao, *Nanoscale Res. Lett.* **2013**, *8*, 430.

[2]   H. Liu, J. Gu, P. D. Ye, *IEEE Electron Device Lett.* **2012**, *33*, 1273.

[3]   S. Chen, S. Kim, W. Chen, J. Yuan, R. Bashir, J. Lou, A. M. Van Der Zande, W. P. King, *Nano Lett.* **2019**, *19*, 2092.